p-FEMs in biomechanics: Bones and Arteries

Zohar Yosibash

Department of Mechanical Engineering, Ben-Gurion University of the Negev, Beer-Sheva, Israel

Abstract

The p-version of the finite element method (p-FEM) is extended to problems in the field of biomechanics: the mechanical response of bones and arteries. These problems are extremely challenging, partly because the constitutive models governing these materials are very complex and have not been investigated by sufficiently rigorous methods. Furthermore, these biological structures have a complex geometrical description (substructures with high aspect ratios), undergo finite deformations (arteries), are anisotropic and almost incompressible (arteries). The intrinsic verification capabilities and high convergence rates demonstrated for linear problems are being exploited and enhanced here, so that validation of the results can be easily conducted by comparison to experimental observations.

In the first part of the paper we present p-FE models for patient-specific femurs generated semi-automatically from quantitative computed tomography (qCT) scans with inhomogeneous linear elastic material assigned directly from the qCT scan. The FE results are being verified and thereafter validated on a cohort of 17 fresh-frozen femurs which were defrosted, qCT-scanned, and tested in an in-vitro setting.

The complex combined passive-active mechanical response of human arteries is considered in the second part and the enhancement of p-FEMs to these non-linear problems is detailed. We apply a new 'p-prediction' algorithm in the iterative scheme and demonstrate the efficiency of p-FEMs compared to traditional commercial h-FEMs as Abaqus (in respect of both degrees of freedom and CPU times). The influence of the active response is shown to be crucial if a realistic mechanical response of an artery is sought.

Email address: zohary@bgu.ac.il (Zohar Yosibash)

Keywords: Femurs, Arteries, Hyperelasticity, p-FEM

1. Introduction

The p-version of the finite element method (p-FEMs), known for three decades already, has several advantages that make its use for linear elliptic problems attractive: the boundary's domain is represented accurately using blending-functions, it converges exponentially for smooth solutions, the finite element mesh is kept constant while only the polynomial degree is increased so that elements are larger, may be far more distorted and have large aspect ratios [1], and is not prone to locking for nearly incompressible materials. These methods have been extended to non-linear problems, first for plasticity [2, 3], and thereafter to isotropic hyperelasticity [4] and to nearly-incompressible hyperelasticity [5].

The intrinsic verification capabilities and high convergence rates of the p-FEMs are extremely important for analysts that aim at validating mathematical models of biomechanical structures such as femurs and arteries. For arteries, this is because the suggested constitutive models at the tissue level are of high mathematical complexity and to determine the coefficients in these models, FE approximations are compared to experimental observations. For femurs, several biomechanical constitutive models at the tissue-level are suggested (formulated based on experiments on small tissue-specimens taken from a whole organ), none of which agreed by the scientific community to best represent the "reality". Therefore, the most appropriate tissue-level model used in the FE analysis of the entire femur is usually sought by comparison to experimental observations, namely, by a validation process. The validation process can only be conducted after the numerical results have been verified, i.e. the numerical error has been quantified. Here, extensions to p-FEMs are addressed to exploit their advantages when solving problems in the field of biomechanics. We first address the mechanical response of a patient-specific human femur, which is well described by an inhomogeneous anisotropic linear elastic model.

Simulations of human femurs by classical h-FEMs started in the early 90's by Keyak and coworkers [6]. In these methods the inhomogeneous distribution of material properties was usually attained by assigning constant distinct values to distinct elements (see e.g. [7] and references therein), thus the material properties become mesh dependent. Furthermore, the bone's surface

was approximated by piecewise flat tessellation or piecewise parabolic tessellation, introducing un-smoothness of the surface and inaccuracies in the surface strains. Among the vast literature addressing h-FE simulations of the femur, the recent ones that present results which are closest to experimental observations are [8, 9].

Combining p-FEMs with quantitative computer tomography (qCT) scans for an individual, a systematic method is presented that generates an accurate description of femur's geometry, creates a p-FE mesh and determines the inhomogeneous material properties. Micro-mechanical approaches can be used to assign orthotropic properties to the whole organ [10, 11, 12], but under simplified loading conditions an isotropic assumption is sufficient to well describe the mechanical response. In this case, the Young's modulus E is determined by empirical relationships to a densitometric measure, and the "best" relationship found to well represent the whole-organ mechanical response is determined based on comparison to experimental observations (the validation process). A solution at increasing polynomial degrees enables an easy verification (both boundary and material properties are smooth so an exponential convergence is obtained), assuring that the numerical errors are bounded by a specified tolerance. Finally, the FE results are compared against all measurable data (strains and displacements) recorded during simplified in-vitro tests on a variety of femurs (with a wide spread in age, gender and weight) for validation. Here, a systematic V&V process, involving the largest set (so far considered) of seventeen human fresh-frozen femurs, is considered. The verified p-FEMs results where then used for validation purposes; both strains and displacements results were compared to experimental observations, such that twelve of these experiments were performed by a different group so a "blind" non-biased comparison was obtained [13].

Unlike bone mechanics, which is governed by the linear theory of elasticity, arteries undergo finite-deformations, are nearly-incompressible, contain families of collagen fibers in different directions, are constructed by two distinct and different thin layers and in addition contain muscle cells that add an active response along their directions. The p-FEM based on the displacement formulation has been shown to be efficient in the framework of finite-deformations for isotropic hyperelastic materials [4, 14] and that it is locking free for nearly-incompressible hyperelastic materials [5, 15] thus it is expected to be especially attractive for modeling arteries.

The fibers reinforced hyperelastic constitutive model (manifested in a

strain energy density function, SEDF) by Holzapfel et. al [16, 17] is complemented by a "compressible" part divided by a bulk modulus because it describes a compressible deformation becoming increasingly more incompressible as the bulk modulus tends to ∞ (see for details [18]). The active response is added to the passive SEDF, derived in [15] based on [19]. A new iterative algorithm, named "p-prediction", is introduced that accelerates considerably the Newton-Raphson method when combined with p-FEMs. The p-FE formulation for anisotropic hyperelastic nearly incompressible "artery-like" domains is described and its advantages over conventional FEMs are demonstrated both when considering degrees of freedom and CPU. Artery-like structures are investigated and the effect of the activation level is demonstrated, showing that the predicted passive-active mechanical response is as observed in experiments.

To demonstrate the advantages of p-FEMs and their systematic use for verification and validation in the field of biomechanics, we construct the manuscript as follows: In section 2 patient-specific p-FE analyses of the femur are presented. We concentrate our attention on the generation of FE models from qCT scans and emphasize the discrete representation of the material data in CT scans and their influence on the numerical results. We also show a systematic V&V process where the verified FE results obtained by a specific constitutive model are compared to a large set of experiments for validation purposes. Thereafter we address artery simulations in section 3 starting by introducing notations, then discuss the constitutive model and weak formulation followed by the discretization in the context of p-FEMs. A simple example problem with an analytical solution is solved by the p-FE implementation to verify the accuracy and efficiency compared to a common commercial h-FE code, Abaqus [20], and thereafter an artery-like cylindrical domain under internal pressure is addressed to investigate the passive-active response when considering collagen and smooth-muscle-cell fibers. We conclude with a summary and conclusions in section 4.

2. *p*-FE analysis of the femur

The generation of CT-based FE models starts with qCT image segmentation that separates the bone region from the remainder of the image based on the Hounsfield Units (HU). To distinguish between the cortical and trabecular regions we associate voxel values of HU$>$ 600 ($\rho_{ash} > 0.6\ g/cm^3$) to

the cortical bone and values of HU$\leq$ 600 to the trabecular bone. Exterior and interior boundaries are traced and arrays are generated, each representing different boundaries of a given slice. These arrays are manipulated by a 3-D smoothing algorithm that generates smooth raw data arrays. The smooth edges, using cubic spline interpolation, are read into the CAD package SolidWorks-2010 (SolidWorks Corporation, MA, USA) and manipulated to generate a surface representation of the femur and subsequently a solid model. Large curved patches representing the surfaces are generated, which are essential in order to allow the automatic p-mesh generator to produce curved-face elements which are not necessary small. The resulting 3D solid is imported into the p-FE StressCheck[1] code. An auto-mesher is thereafter applied that generates tetrahedral high-order elements having curved faces, following exactly the domain's geometry. The entire algorithm (qCT to FE) is schematically illustrated in Figure 1.

Remark 1. The numerical error associated with the use of tetrahedron p-elements, compared to hexahedral p-elements, was investigated and was confirmed to be of the same order of accuracy when the polynomial degree is increased [21]. The "overly stiff" behavior of tetrahedral h-elements does not occur for p-FEs.

2.1. Assigning isotropic material properties to the finite elements

The next step is to assign inhomogeneous material properties to the finite elements, associated with the density at each point within the bone. Since the material properties are given at distinct "grid" points, at the center of the qCT voxels, we demonstrate here on a benchmark problem that for a reasonably "dense grid" an excellent approximation is obtained as if the material properties would had been available as an analytic function.

2.1.1. A benchmark problem to quantify the influence of E-data provided at discrete points

Consider a sphere determined by

$$\Omega = \left\{ (r, \varphi, \theta) \;\middle|\; r < 5,\ \varphi < \pi,\ \theta < 2\pi \right\}$$

[1]StressCheck is trademark of Engineering Software Research and Development, Inc, St. Louis, MO, USA.

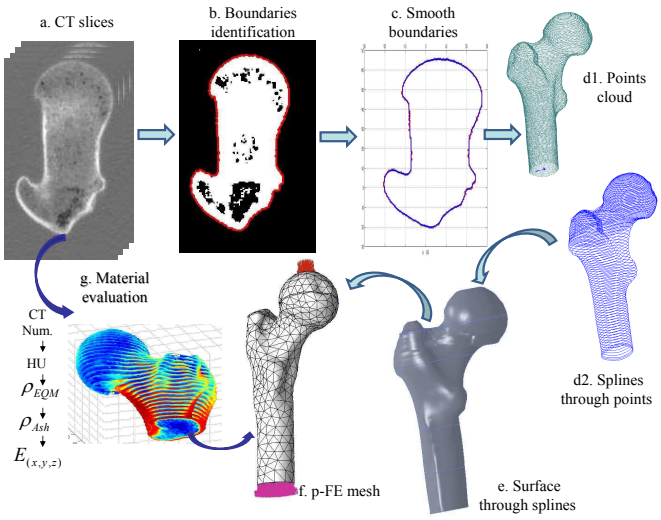

Figure 1: Schematic flowchart describing the generation of the p-FE model from qCT scans. a - Typical CT-slice, b. - Contour identification, c. - Smoothing boundary points, d1. - Points cloud representing the bone surface. d2. - Close splines for all slices, e. - Bone surface, f. - p-FE mesh and g. - Material evaluation from CT data. (Figure from [12].)

where $r = \sqrt{x^2 + y^2 + z^2}$, with a boundary $\partial\Omega$ defined by $r = 5$ (see Figure 2). The center of the sphere is at $(x, y, z) = (0, 0, 0)$.
Traction boundary conditions: On the part of the boundary $\partial\Omega_T$ defined by $r = 5 \cap \{z > 4\}$ pressure boundary conditions $t_n = -1/\partial\Omega_T$ are prescribed. On $\partial\Omega_{T_0}$ defined by $r = 5 \cap \{-4 < z < 4\}$ traction free boundary conditions are prescribed.
Clamped boundary conditions: On the part of the boundary $\partial\Omega_u$ defined by $r = 5 \cap \{z < -4\}$ clamped boundary conditions are prescribed $\boldsymbol{u} = (u_x, u_y, u_z)^T = \mathbf{0}$.
Material properties: Consider an inhomogeneous isotropic material with Young's modulus E being provided analytically:

$$E = 100 \times \left[1 + \sin(r\pi/10) + exp(r^2/10)\right] + 100x + 100y. \qquad (1)$$

This expression is a good representation of a bone-like structure which has a low Young's modulus in the middle, that becomes higher towards the surface.

The last two terms in (1) ensure that the material properties do not have a spherical symmetry. To represent a CT-like scan of such a sphere, the analytical expression is evaluated at voxels with increasing resolution. Three resolutions denoted as 50 Cells, 100 Cells and 150 Cells resemble a CT scan in a bounding box of dimensions $11 \times 11 \times 11$ so that $\{-5.5 \geq x, y, z \geq 5.5\}$. This box containing the sphere is divided into $50 \times 50 \times 50$, $100 \times 100 \times 100$ and $150 \times 150 \times 150$ voxels and E according to (1) is computed in the middle of each voxel within the sphere. These discrete values are provided in the FE analysis, and are typical of the resolutions in CT-scans. In all cases the Poisson's ratio is kept constant $\nu = 0.3$. The domain was discretized by 128 p-FEs (tetrahedrons, pentahedrons and hexahedrons) as shown in Figure 2 with the boundary conditions and E distribution.

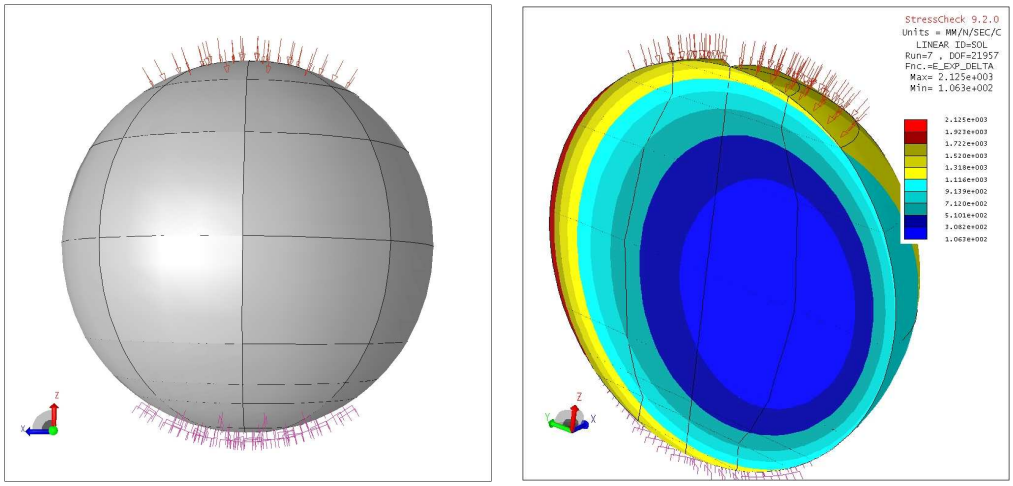

Figure 2: Left - FE mesh and BCs. Right - Inhomogeneous Young's modulus at a slice at $x = 0$.

The total potential energy, the displacement in the z direction at the apex ($u_z(0, 0, 5)$), and the maximum negative average principal strain ε_3 at 100 points along the surface curve between $z = 4$ to $z = 4.75$ shown in Figure 3 for polynomial degrees $p = 1$ to 8 are summarized in Table 1.

The relative error as percentage in the potential energy *compared to* $p = 8$ *FE solution with the "analytic E"* is presented in Figure 4.

The convergence in energy norm for increasing p values is rather slow. This is because the solution at the circular edge $r = 5 \cup z = -4$, which is the curve where a sharp transition in boundary conditions occurs (from clamped

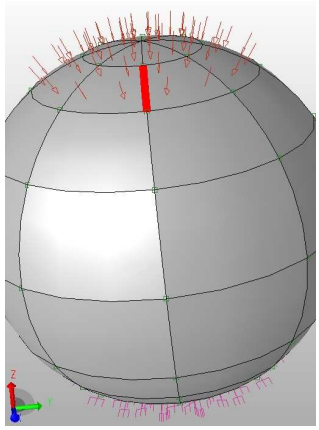

Figure 3: The edge along which ε_3 is extracted and then averaged.

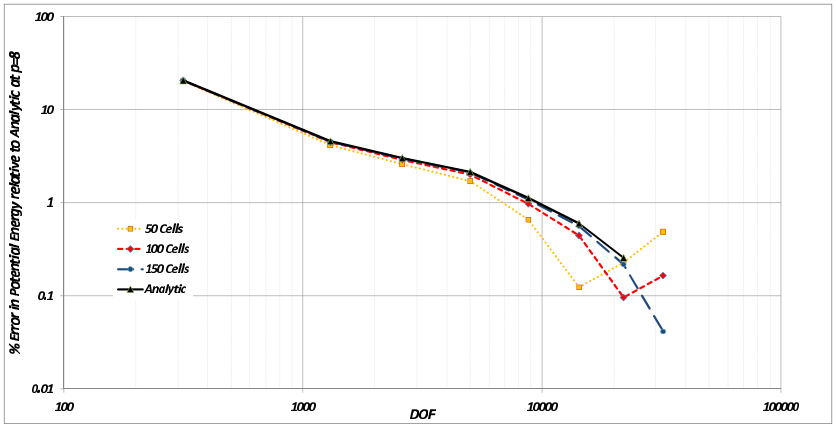

Figure 4: Relative error as percentage in potential energy compared to the FE analysis with analytical E at $p = 8$.

Table 1: FE results for the sphere problem: p-level, DOFs, potential energy, $u_z(0,0,5)$ and average ε_3 for the E given at 50,100,150 CT-like cells and the analytic E.

		Total Potential Energy				u_z			
p	DOF	50 Cells	100 Cells	150 Cells	Analytic	50 Cells	100 Cells	150 Cells	Analytic
1	315	-1.435E-4	-1.431E-4	-1.430E-4	-1.429E-4	-3.833E-4	-3.822E-4	-3.818E-4	-3.817E-4
2	1302	-1.727E-4	-1.721E-4	-1.720E-4	-1.719E-4	-4.310E-4	-4.302E-4	-4.296E-4	-4.296E-4
3	2601	-1.755E-4	-1.750E-4	-1.748E-4	-1.747E-4	-4.341E-4	-4.337E-4	-4.331E-4	-4.330E-4
4	5004	-1.771E-4	-1.765E-4	-1.764E-4	-1.763E-4	-4.379E-4	-4.369E-4	-4.362E-4	-4.362E-4
5	8775	-1.790E-4	-1.784E-4	-1.782E-4	-1.781E-4	-4.415E-4	-4.404E-4	-4.399E-4	-4.398E-4
6	14298	-1.799E-4	-1.794E-4	-1.792E-4	-1.791E-4	-4.433E-4	-4.425E-4	-4.418E-4	-4.418E-4
7	21957	-1.806E-4	-1.800E-4	-1.798E-4	-1.797E-4	-4.446E-4	-4.439E-4	-4.431E-4	-4.431E-4
8	32136	-1.811E-4	-1.805E-4	-1.802E-4	-1.802E-4	-4.458E-4	-4.447E-4	-4.441E-4	-4.441E-4

		Average ε_3			
p	DOF	50 Cells	100 Cells	150 Cells	Analytic
1	315	-2.166E-5	-1.756E-5	-2.166E-5	-2.150E-5
2	1302	-2.141E-5	-2.029E-5	-2.141E-5	-2.132E-5
3	2601	-2.139E-5	-2.077E-5	-2.139E-5	-2.125E-5
4	5004	-2.130E-5	-2.143E-5	-2.130E-5	-2.124E-5
5	8775	-2.119E-5	-2.150E-5	-2.119E-5	-2.124E-5
6	14298	-2.135E-5	-2.164E-5	-2.135E-5	-2.135E-5
7	21957	-2.129E-5	-2.172E-5	-2.129E-5	-2.139E-5
8	32136	-2.130E-5	-2.179E-5	-2.130E-5	-2.143E-5

to traction free), is singular, i.e. the stresses tend to infinity. A remedy to this deterioration in the convergence rate may be achieved in the framework of p-FEMs, if a mesh refinement in geometric progression towards the singular circular edge is enforced (see [1]). Nevertheless, for comparison purposes between the analytic E and voxelized E the slow convergence should not pose a problem. One is interested whether the voxelized E description represents well the analytic E. The presented benchmark problem demonstrates well that the CT-like E values provide an approximation, comparable in quality to the material properties being specified by analytic functions. In Figure 4 a fast convergence in potential energy is observed (when comparing the the voxelized results to the analytical ones).

2.1.2. E in a patient-specific femur determined by empirical correlation

Many empirical relations between Young's modulus and bone density, with a constant Poisson's ratio were suggested, see e.g. [22, 23, 24, 25, 26]. In [21, 27] we found that p-FE analyses with the relationships in [24] (the cortical connections are based on [25]) provide the closest results to in-vitro

experiments on the proximal femur:

$$\rho_{EQM} = 10^{-3}\,(a \times HU - b) \quad [g/cm^3] \tag{2}$$
$$\rho_{ash} = (1.22 \times \rho_{EQM} + 0.0523) \quad [g/cm^3] \tag{3}$$
$$E_{Cort} = 10200 \times \rho_{ash}^{2.01} \quad [MPa] \quad \rho_{ash} > 0.6 \tag{4}$$
$$E_{Trab} = 5307 \times \rho_{ash} + 469 \quad [MPa] \quad 0.27 < \rho_{ash} \leq 0.6 \tag{5}$$
$$E_{Trab} = 33900 \times \rho_{ash}^{2.20} \quad [MPa] \quad \rho_{ash} \leq 0.27 \tag{6}$$

where ρ_{EQM} is the equivalent mineral density, ρ_{ash} is the ash density, E_{Cort}, E_{Trab} are the Young's modulii in the cortical and trabecular regions and the parameters a and b are determined by K_2HPO_4 phantoms placed around the femur in the CT-scan. Constant Poisson ratio $\nu = 0.3$ was assigned to the entire bone. According to a sensitivity analysis in [28, 21] the influence of ν on the results is very small.

Determination of $E(x, y, z)$ at each integration point (Gauss points), in the FE model is performed as follows. First a moving average algorithm is applied to average the HU data in each voxel based on a pre-defined cubic volume of $3 \times 3 \times 3$ mm^3 surrounding it (cubic volumes of 27,125,343 mm^3 showed similar results in [28]). HU averaged data is subsequently converted to an equivalent mineral density ρ_{EQM} by (2) which is determined by the calibration phantom - see for details [29, 28]. E at every Gauss point is assigned the value of the closest available point in the qCT file. The number of Gauss points was 512 for tetrahedral and 2744 for hexahedral elements, independent of the p-level.

2.1.3. Verification of p-FE results and sensitivity analyses.

p-FE results are verified so to ensure that the numerical error is under a specific tolerance. To this end, the polynomial degree over the elements is increased until the relative error in energy norm is small, and the strains at the points of interest converge. Such a verification, for example for a femur denoted FF3, when increasing p from 1 to 5 is presented in Figure 5.

The solid model of the femur was partitioned such that the number of finite elements was between 3500 to 4500 elements ($\sim 150,000$ degrees of freedom (DOFs) at $p = 4$ and $\sim 300,000$ DOFs at $p = 5$).

Sensitivity studies:

To ensure the reliability of the FE analyses sensitivity studies were performed to ensure that the obtained results are not too sensitive. a) Poisson

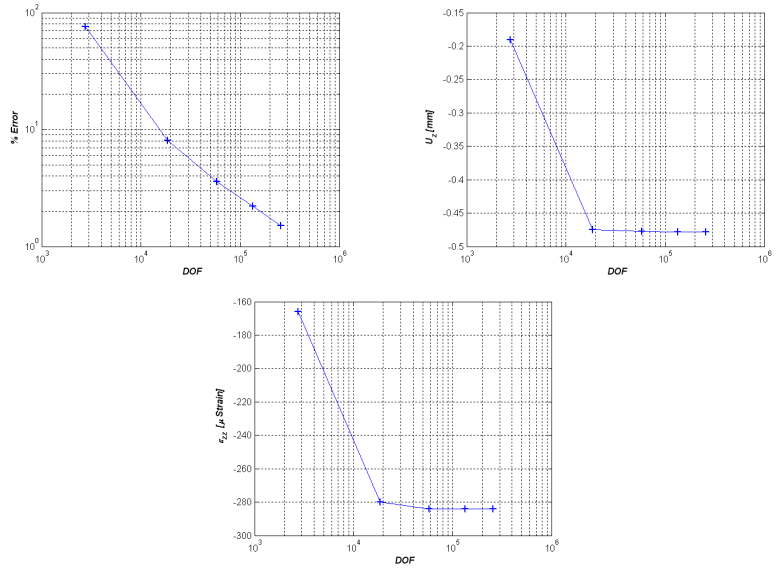

Figure 5: Convergence in energy norm, head displacement and ϵ_{zz} at a representative point of interest in FF3. (Figure from [27].)

ratios $\nu = 0.01, 0.1, 0.3, 0.4$ were applied to the femur, as in [23, 30, 28], b) The distal face of the femur residing in PMMA in in-vitro experiments was either clamped or modeled as attached to a distributed spring. c) Strains at strain-gauge locations were checked at $\pm 5^\circ$ offset orientations. d) Strains were computed either as averaged over an element or as maximum or minimum values.

2.2. Validation by comparison to in-vitro experiments

Biomechanical experiments on seventeen fresh-frozen human cadaver femurs were conducted to validate the FEA. Experiments on five femurs (denoted FF1-FF5) were performed in-house, and six pairs of femurs (denoted by 1 to 6) were tested by another research institute with results unknown until the analyses were completed to avoid any bias. Table 2 summarizes the data on femurs and CT scan resolutions. Within one day of defrosting and performing CT measurements, experiments were conducted to mimic a simple stance position configuration in which the femurs were loaded through their head while inclined at different inclination angles (0, 7, 15 and 20 degrees) as shown in Figure 6. We measured the vertical and horizontal displacements

Table 2: Data of femurs and CT scan resolution.

Donor label	Side	Age (years)	Height (cm)	Weight (kg)	Gender	Slice thickness (mm)	Pixel size (mm)	Load rate (mm/sec)
1	L & R	59	180	96	female	1.00	0.547	1/6
2	L & R	53	193	98	male	1.00	0.488	1/6
3	L & R	48	170	55	male	1.00	0.488	1/6
4	L & R	64	168	136	female	1.00	0.488	1/6
5	L & R	54	178	161	male	1.00	0.547	1/6
6	L & R	58	185	86	male	1.00	0.547	1/6
FF1	L	30	N/A	N/A	male	0.75	0.78	1/600-1/30
FF2	R	20	N/A	N/A	female	1.5	0.73	1/600, 1/120, 1/6
FF3	L	54	N/A	N/A	female	1.25	0.52	1/2
FF4	R	63	N/A	N/A	male	1.25	0.195	1/60, 1/6, 1
FF5	R	56	N/A	N/A	male	1.25	0.26	1/2

of femur's head, the strains at the inferior and superior parts of the neck, and on the medial and lateral femoral shaft. In all experiments a linear response between force and displacements and strains was observed beyond 200N preload. The experimental error is within a $\pm 5\%$ range (details are provided in [21, 27, 12]).

Figure 6: Typical experiments on FF1-FF5 at 0^o and 20^o inclination angles. Right - Representative strain gauges location at the neck and shaft regions.

On the six pairs 1-6 five uniaxial strain-gauges (SGs) were bonded and

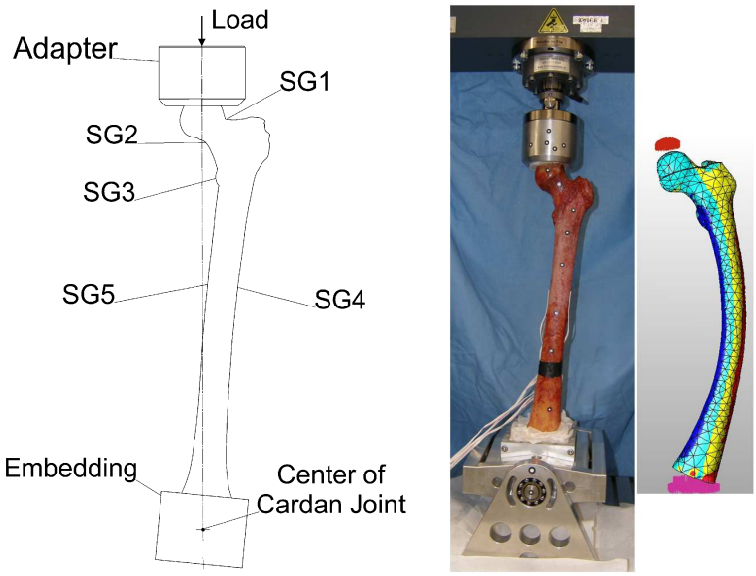

Figure 7: (a-left) Sketch of the frontal plane of an embedded and instrumented left femur. The adapter applied the load by the testing machine to the specimen. The proximal embedding (hidden in adapter) builds a ball-joint with the adapter. Strain gauges (SG1-SG5) are applied to specific anatomic sites. SG1 - located at the middle of the superior neck. SG2 - located opposite to SG1 at the inferior neck. SG3 - located next to the most prominent part of the lesser trochanter. SG4 - located 100mm distally to SG3 at the medial side of the shaft. SG5 - located opposite to SG4 at the lateral side of the shaft. (b-right) Experimental setup with the optical markers on an instrumented left femur and its corresponding deformed (magnified) FE model (Figure from [13].)

optical markers were distributed over the femur, the adapter of the testing machine, and the cardan joint, see Figure 7. The distal end of each femur was potted with casting resin in an aluminum case that fitted into a cardan joint so that the line of force went through the center of the femoral head and the center of the epicondyles. The femoral head was potted in a hemisphere of casting resin that fitted the proximal adapter of the test setup (Fig. 7b). The mean values of strains were calculated to be used for the later comparison with the FEA. The total displacements $u_{tot} = \sqrt{u_x^2 + u_y^2 + u_z^2}$ of the optical markers on the bone surface were also calculated. Details on these experiments were provided in [13].

The verified FE analyses that mimic the in-vitro experiments are used for validation purposes, i.e. to ensure that these indeed represent the biome-

chanical response. For each FE analysis the strains at the location of the strain-gauges (SGs) were averaged over a small area representing the area over which the gauge or the SG measured the strains. Because uni-axial SGs were used in our experiments, we considered the FE-strain component in the direction coinciding with the SG direction (in most cases the SGs are aligned along the principal strain directions). A total of 102 displacements and 161 strains on the 17 femurs were used to assess the validity of the p-FE simulations. In Figure 8 the pooled FE strains and displacements are compared to the experimental observations - this comparison is demonstrated by a linear regression plot, inspecting the slope, intersection and R^2 of the linear regression between the experimental observations and FE predictions.

Remark 2. Note that for twelve of the seventeen femurs a blind comparison was performed, i.e. the group that performed the experiments did not know the FE results, and vice-versa, the experimental results were not known by the group that performed the analysis.

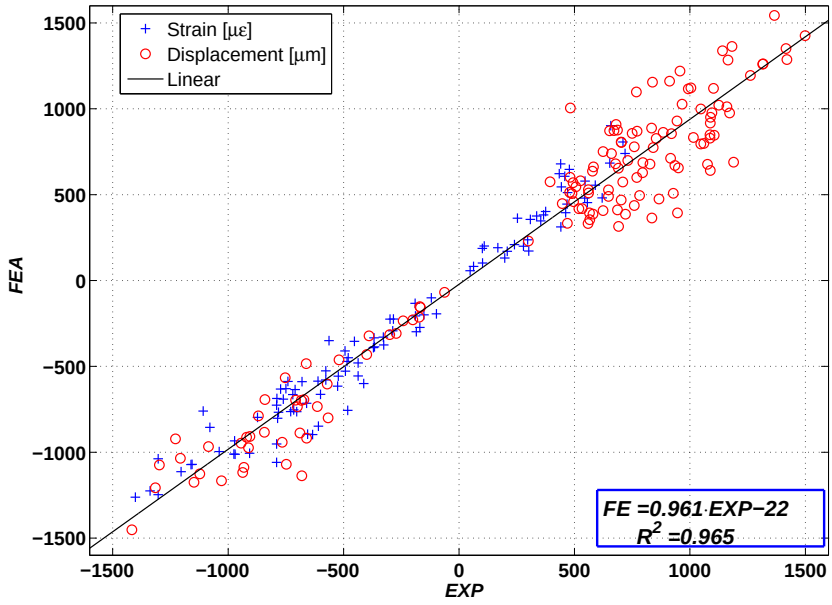

Figure 8: Comparison of the computed strains + and displacements ○ to the experimental observations normalized to 1000 N load.

One may observe the unprecedented match between the predicted and measured data for femurs under stance position loading: the slope and R^2 of the linear regression are very close to 1. The strains prediction is highly accurate, but not less important, the displacements are also well predicted.

Based on the results of validation experiments no reasons were found to reject or modify the mathematical model, so that the FE results may be also utilized to investigate the internal state of strains within the femur. For example, Figure 9 shows the maximum (tensile) and minimum (compression) principal strains at a cutting plane within FF5.

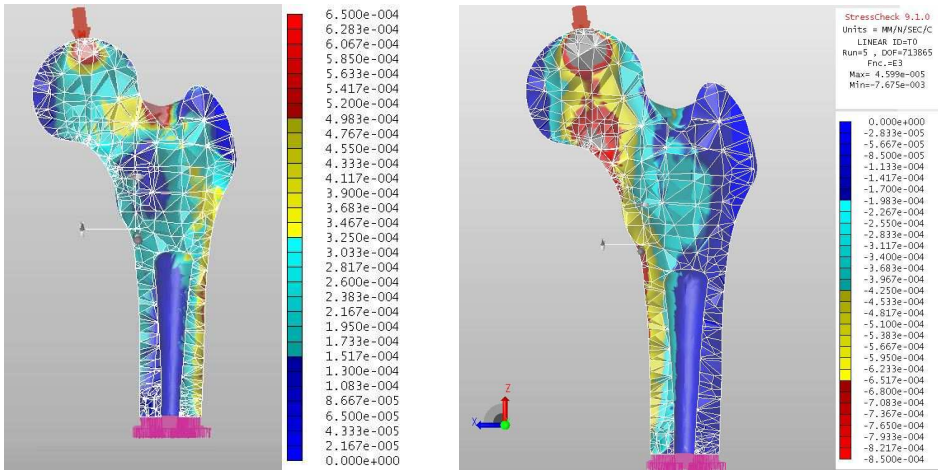

Figure 9: Principle maximum strains (left) and minimum strains (right) at a cutting plane in the middle of FF5, loaded at 7^o.

The presented p-FEMs based on patient-specific qCT-scans are semiautomatic procedures requiring less than three hours from qCT-scan to the verified results on a PC. The ability to keep numerical errors under control enables to focus the attention on the idealization errors. The validation of the FE-results was performed by comparing FE extracted strains *and* displacements to measured data on 17 fresh-frozen femurs. This comparison demonstrated an excellent agreement, better than previous works reported in the literature (comparison of displacements is not reported in studies by other authors, to the best of our knowledge).

Thanks to the double-blinded validation on 12 of the 17 femurs [13], this validation process is also bias-free. The V&V process outlined herein lays the foundation for the extension of the study to prediction of fractures in

pathological cases as osteoporotic bones. Once the strains and displacements are shown to be well computed in the femur, these can be used so to determine the predictability of different failure laws. This of course calls for a new validation process along the lines outlined herein.

The successful use of p-FEMs in biomechanical problems governed by linear elasticity and the systematic use of a V&V methodology are expected to be more pronounced when the equations are non-linear, as the governing equations describing the mechanical response of arteries. In the next section the application of p-FEMs for simulating artery's mechanical response is addressed and verified towards its validation by experimental observations.

3. *p*-FEMs for arteries

The constitutive models for arteries are based on fiber reinforced, nearly-incompressible hyperelasticity, involving finite deformations, as detailed in Appendix A. Because both passive and active responses are of major importance for the mechanical response of the artery tissue, we consider a strain-energy density function (SEDF) of the form:

$$\Psi_{tissue} = \Psi_{passive} + \Psi_{active} \tag{7}$$

The passive SEDF (see (A.4) and (A.6) in the Appendix) represents an isotropic nearly-incompressible hyperelastic matrix with two families of fibers which depends on the invariants of the right Cauchy-Green tensor $\boldsymbol{C}$ and two unit direction vectors along collagen fiber directions $\hat{\boldsymbol{M}}_0$, and $\hat{\boldsymbol{M}}_1$. For example, using the Cartesian coordinate system in Figure 10, the fibers directions are
$\hat{\boldsymbol{M}}_0 = (\sin\beta_M, -\cos\beta_M \frac{Y}{\sqrt{Y^2+Z^2}}, \cos\beta_M \frac{Z}{\sqrt{Y^2+Z^2}})^T$,
$\hat{\boldsymbol{M}}_1 = (-\sin\beta_M, -\cos\beta_M \frac{Y}{\sqrt{Y^2+Z^2}}, \cos\beta_M \frac{Z}{\sqrt{Y^2+Z^2}})^T$. The active SEDF Ψ_{active} depends on the concentration level of a vasoconstrictor, the stretch ratio and a unit direction vector along the smooth muscle cells, given in (A.10).

3.1. Weak formulation and discretization by p-FEMs

Having determined the SEDFs, we choose to formulate a weak formulation in the reference configuration, neglecting inertia terms (also denoted by the Total-Lagrange formulation), see e.g. [31]. This is a Newton-Raphson iterative scheme in which the displacements are assumed to be known at a

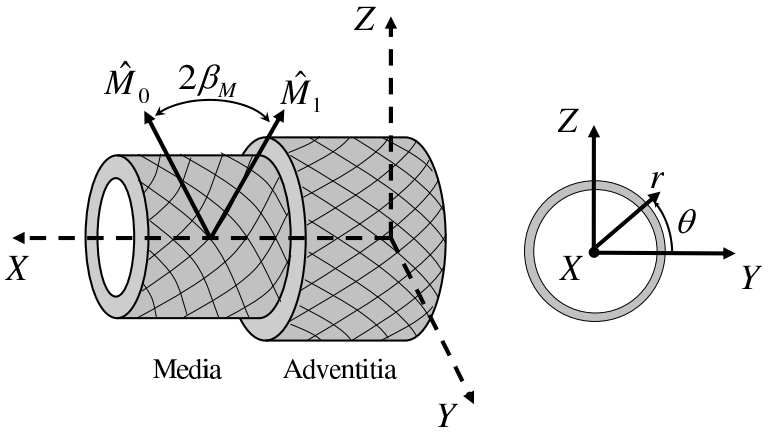

Figure 10: Coordinate system in a typical artery. (Figure from [18].)

given instance, $\boldsymbol{U}^{(k)}$, so that when applying an additional load increment, one is interested in the associated displacement increment denoted by $\Delta\boldsymbol{U}$. Once $\Delta\boldsymbol{U}$ is computed a new displacement vector is generated

$$\boldsymbol{U}^{(k+1)} = \boldsymbol{U}^{(k)} + \Delta\boldsymbol{U}, \tag{8}$$

and the iterative scheme continues until convergence.

Having $\boldsymbol{U}^{(k)}$, the associated deformation gradient may be computed $\boldsymbol{F}^{(k)} \overset{\text{def}}{=} \boldsymbol{I} + \frac{\partial \boldsymbol{U}^{(k)}}{\partial \boldsymbol{X}}$. The linearized system to be solved is [31, p.148]:

$$\text{Find } \Delta\boldsymbol{U} \in \mathcal{E}(\Omega_0) \;\; \text{such} \;\; \text{that } \forall \boldsymbol{Q} \in \mathcal{E}(\Omega_0)$$

$$\begin{aligned}
&\frac{1}{4}\int_{\Omega_0} \left[\frac{\partial \boldsymbol{Q}}{\partial \boldsymbol{X}} \cdot \boldsymbol{F}^{(k)} + \boldsymbol{F}^{(k)} \cdot \frac{\partial \boldsymbol{Q}}{\partial \boldsymbol{X}}\right] : \mathbb{C}^{(k)} : \left[\frac{\partial \Delta\boldsymbol{U}}{\partial \boldsymbol{X}} \cdot \boldsymbol{F}^{(k)} + \boldsymbol{F}^{(k)} \cdot \frac{\partial \Delta\boldsymbol{U}}{\partial \boldsymbol{X}}\right] d\Omega_0 \\
&\qquad + \int_{\Omega_0} \boldsymbol{S}(\boldsymbol{U}^{(k)}) : \left(\frac{\partial \Delta\boldsymbol{U}}{\partial \boldsymbol{X}} \cdot \frac{\partial \boldsymbol{Q}}{\partial \boldsymbol{X}}\right) d\Omega_0 + DG(\Delta\boldsymbol{U}, \boldsymbol{Q}) \\
&= \int_{\partial\Omega_0} \boldsymbol{T}^{(N)} \cdot \boldsymbol{Q} d\Gamma_0 + G(\boldsymbol{Q}) \\
&\qquad - \frac{1}{2}\int_{\Omega_0} \boldsymbol{S}(\boldsymbol{U}^{(k)}) : \left[\left(\frac{\partial \boldsymbol{Q}}{\partial \boldsymbol{X}}\right) \cdot \boldsymbol{F}^{(k)} + \left(\boldsymbol{F}^{(k)}\right) \cdot \frac{\partial \boldsymbol{Q}}{\partial \boldsymbol{X}}\right] d\Omega_0
\end{aligned} \tag{9}$$

with $\boldsymbol{T}^{(N)} = \boldsymbol{F}\boldsymbol{S}\cdot\hat{\boldsymbol{N}}$ being the traction applied on the reference configuration boundary. The second Piola-Kirchhoff stress tensor and fourth order tangent tensor are obtained from the SEDF:

$$\boldsymbol{S} \stackrel{\text{def}}{=} 2\frac{\partial \Psi}{\partial \boldsymbol{C}}, \quad \mathbb{C} \stackrel{\text{def}}{=} 2\frac{\partial \boldsymbol{S}}{\partial \boldsymbol{C}} \tag{10}$$

$$\boldsymbol{S} = \boldsymbol{S}_{passive} + \boldsymbol{S}_{active} = 2\frac{\partial \Psi_{passive}}{\partial \boldsymbol{C}} + 2\frac{\partial \Psi_{active}}{\partial \boldsymbol{C}}, \tag{11}$$

$$\mathbb{C} = \mathbb{C}_{passive} + \mathbb{C}_{active} = 2\frac{\partial \boldsymbol{S}_{passive}}{\partial \boldsymbol{C}} + 2\frac{\partial \boldsymbol{S}_{active}}{\partial \boldsymbol{C}} \tag{12}$$

The terms $DG(\Delta\boldsymbol{U}, \boldsymbol{Q})$ and $G(\boldsymbol{Q})$ are to be added if pressure (follower loads) are considered, see equations (49) and (53) in [14].

Remark 3. In our in-house p-FEM implementation $\mathbb{C}$ is computed at each iteration step, unlike the modified Newton methods in which $\mathbb{C}$ is computed only once for each load increment or once every several equilibrium iterations.

3.1.1. p-FEM implementation

The weak form (9) is discretized using a space of hierarchical polynomials (shape functions) $N_i(\xi, \eta, \zeta)$ on the standard hexahedral element (see [32]). The sought (trial) vector $\Delta\boldsymbol{U}$ is represented by an unknown $3n \times 1$ vector $\Delta\hat{\boldsymbol{U}}$ as follows:

$$\Delta\boldsymbol{U} = \begin{bmatrix} N_1 \cdots N_n & 0 \cdots 0 & 0 \cdots 0 \\ 0 \cdots 0 & N_1 \cdots N_n & 0 \cdots 0 \\ 0 \cdots 0 & 0 \cdots 0 & N_1 \cdots N_n \end{bmatrix} \Delta\hat{\boldsymbol{U}} \stackrel{\text{def}}{=} [N]\Delta\hat{\boldsymbol{U}} \tag{13}$$

whereas $\boldsymbol{Q} \stackrel{\text{def}}{=} [N]\hat{\boldsymbol{Q}}$ is the test vector. Using blending mapping functions $\Gamma(\xi, \eta, \zeta)$ from the standard element to the physical element [1], an *exact geometry description of the faces and edges* of the physical element is obtained:

$$\boldsymbol{X} = \begin{Bmatrix} X \\ Y \\ Z \end{Bmatrix} = \begin{Bmatrix} \Gamma_1(\xi, \eta, \zeta) \\ \Gamma_2(\xi, \eta, \zeta) \\ \Gamma_3(\xi, \eta, \zeta) \end{Bmatrix}, \quad [\mathcal{J}] = \begin{bmatrix} \frac{\partial \Gamma_1}{\partial \xi} & \frac{\partial \Gamma_2}{\partial \xi} & \frac{\partial \Gamma_3}{\partial \xi} \\ \frac{\partial \Gamma_1}{\partial \eta} & \frac{\partial \Gamma_2}{\partial \eta} & \frac{\partial \Gamma_3}{\partial \eta} \\ \frac{\partial \Gamma_1}{\partial \zeta} & \frac{\partial \Gamma_2}{\partial \zeta} & \frac{\partial \Gamma_3}{\partial \zeta} \end{bmatrix} \tag{14}$$

Derivatives of the shape functions in the standard element are computed by:

$$\frac{\partial N_i}{\partial \boldsymbol{X}} = \begin{Bmatrix} \frac{\partial N_i}{\partial X} \\ \frac{\partial N_i}{\partial Y} \\ \frac{\partial N_i}{\partial Z} \end{Bmatrix} = [\mathcal{J}]^{-1} \begin{Bmatrix} \frac{\partial N_i}{\partial \xi} \\ \frac{\partial N_i}{\partial \eta} \\ \frac{\partial N_i}{\partial \zeta} \end{Bmatrix} \tag{15}$$

Remark 4. It is important to realize that the use of the Total-Lagrange formulation does not require to update the FE mesh, and hence the Jacobian $[\mathcal{J}]$ is determined once, relative to the material (undeformed) configuration. The updates from one iteration to the next are performed by updating the integrand terms due to the update of the displacements (8).

By using (15) with (13) and (14) the discretized form of (9), to be solved at each iteration step, is obtained:

$$\left[K^{Tangent}\right] \Delta\hat{U} = \boldsymbol{r}^{ob} \tag{16}$$

The tangent stiffness matrix, $[K^{Tangent}]$, consists three parts $[K^{Tangent}] = [K_T^{Int,Mat} + K_T^{Int,Geo} + K_T^{Follower}]$ [31] with the third term (see [14, eq. (53)]) only considered in cases of follower loads.
The out-of-balance vector, $\boldsymbol{r}^{ob}$ consists also three parts $\boldsymbol{r}^{ob} = \boldsymbol{r}^{Ext} + \boldsymbol{r}^{Follwer} - \boldsymbol{r}^{Int}$ with $\boldsymbol{r}^{Follwer}$ (given in [14, eq. (49)]) only considered in case of follower loads.

The explicit expressions for the computation of $\boldsymbol{r}^{ob}$ and $[K^{Tangent}]$ are presented in [18]. Both $\boldsymbol{r}^{ob}$ and $[K^{Tangent}]$ are computed at each iteration and the iterative process continues until the relative difference in each element of the "out-of-balance" vector, $\left|\boldsymbol{r}_i^{ob(k)} - \boldsymbol{r}_i^{ob(k-1)}\right| / \left|\boldsymbol{r}_i^{ob(k)}\right|$, is smaller than a given tolerance, $\epsilon = 10^{-6}$.

Remark 5. The matrices $[K^{Int,Mat}]$ and $[K^{Int,Geo}]$ are symmetric [31] whereas $[K^{Follower}]$ in general is not [31]. Therefore the bi-conjugate gradient method [33] is utilized for inverting $[K^{Tangent}]$ and solving (16).

3.1.2. Acceleration of the iterative scheme by "p-prediction"

The Newton-Raphson iterative scheme requires an initial guess in the vicinity of the solution, and the closer this guess is to the exact solution, the faster is the convergence (the number of iterations are smaller). It is common therefore, in most FE implementation to introduce an additional loop by dividing the total load into several load steps, so that the iterations on $\boldsymbol{U}^{(k)}$ start at each load step with an initial solution being the solution at the previous load step.

The p-FE inherent hierarchical basis of the shape functions allows a simple and novel acceleration of the iterative scheme by predicting the initial guess

$\boldsymbol{U}^{(0)}$ for a higher p-level using the converged solution already available at a lower p-level. This "p-prediction" method requires load steps only for $p = 1$ with an "usual" Newton-Raphson iterative scheme. For $p \geq 2$ the converged solution at $p - 1$ is used as the "initial guess" to the iterative scheme. This results in a very fast convergence, noticed to be obtained within one load step in all numerical tests. Numerical experiments using the standard and "p-prediction" methods show a speedup factor of at least 20 in CPU. For a nearly-incompressible material, the p-FEMs are locking-free only for p-levels 4 and above [5], therefore the first initial solution to be applied with the "p-prediction" method is at $p = 4$.

3.2. Verification of the p-FE implementation

To verify our in-house numerical implementation and to compare its efficiency to classical h-FEMs, we first consider a benchmark problems for which an analytical solution was provided for a hyperelastic material in [18]. Consider the cube defined by $\Omega = \left\{ (X, Y, Z) \;\middle|\; 0 < X < 2,\ 0 < Y < 2,\ 1 < Z < 3 \right\}$ shown in Figure 11 with the constitutive model given by the SEDF $\Psi = \Psi_{isoch} + \Psi_{vol}$ in (A.4). We apply the following boundary conditions on

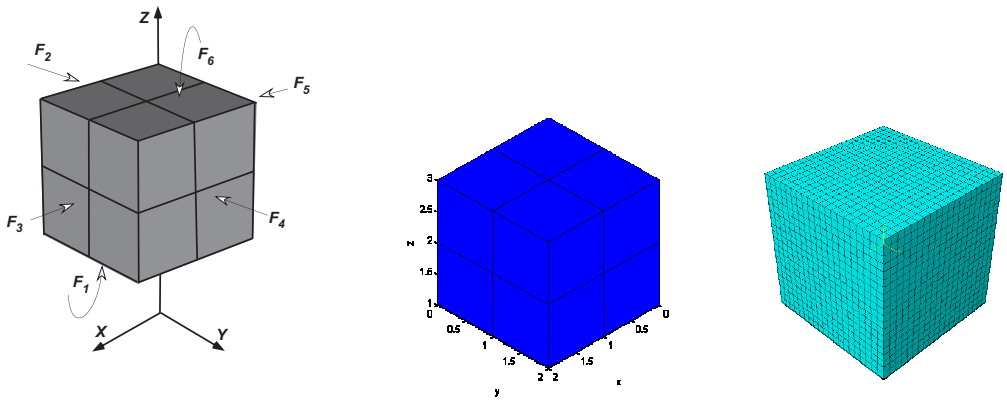

Figure 11: Domain and p-FE mesh for the cube problem and h-FE mesh used by Abaqus.

the six faces $F1 - F6$:

$$\begin{cases} \boldsymbol{U} = \boldsymbol{0} & \text{on } F_1 \\ t_X = 0, \quad t_Y = -\left[\frac{2}{3}c_1\left(Z^{-\frac{1}{3}} - Z^{\frac{2}{3}}\right) + \frac{2}{D_1}\left(Z - \sqrt{Z}\right)\right], \quad t_Z = 0 & \text{on } F_2 \\ t_X = \frac{2}{3}c_1\left(Z^{-\frac{1}{3}} - Z^{\frac{2}{3}}\right) + \frac{2}{D_1}\left(Z - \sqrt{Z}\right), \quad t_Y = 0, \quad t_Z = 0 & \text{on } F_3 \\ t_X = 0, \quad t_Y = \frac{2}{3}c_1\left(Z^{-\frac{1}{3}} - Z^{\frac{2}{3}}\right) + \frac{2}{D_1}\left(Z - \sqrt{Z}\right), \quad t_Z = 0 & \text{on } F_4 \\ t_X = -\left[\frac{2}{3}c_1\left(Z^{-\frac{1}{3}} - Z^{\frac{2}{3}}\right) + \frac{2}{D_1}\left(Z - \sqrt{Z}\right)\right], \quad t_Y = 0, \quad t_Z = 0 & \text{on } F_5 \\ t_X = 0, \quad t_Y = 0, \quad t_Z = \frac{8}{9}c_1 3^{\frac{1}{6}} + \frac{2}{D_1}\left(\sqrt{3} - 1\right) & \text{on } F_6, \end{cases}$$

and the body forces:

$$(f_X, f_Y, f_Z) = \left(0,\ 0,\ -\frac{10}{9}c_1 Z^{-\frac{7}{3}} + \frac{2}{9}c_1 Z^{-\frac{4}{3}} - \frac{1}{D_1 Z}\right).$$

Under these boundary conditions the exact solution is (notice that the solution is analytic because the domain is such that $1 < Z$):

$$x = X,\ y = Y,\ z = \frac{1}{3}\left(2Z^{\frac{3}{2}} + 1\right)$$

or in terms of displacements: $U_X = U_Y = 0, \quad U_Z = \frac{1}{3}\left(2Z^{\frac{3}{2}} + 1\right) - Z$

The material properties chosen are $c_1 = 0.027$ MPa and $D_1 = 30$ MPa^{-1}. The "cube problem" was solved by the p-FEM with eight uniform hexahedral elements and for comparison also by the h-FE commercial code Abaqus 6.8 EF with 8-node hexahedral elements and an automatic load step control (the conventional "displacement formulation elements" were used in Abaqus because the deformation is clearly compressible). Structured meshes of hexahedral elements are used for all analyses on arteries reported here. A direct solver was used for both codes, and computations performed on a single processor (no parallelization was applied).

The convergence pattern is shown in Figure 12 by monitoring the relative error in energy norm, defined as:

$$||e(\mathcal{U})||(\%) = \sqrt{\frac{\int_\Omega \Psi(\boldsymbol{C})d\Omega_{FE} - \int_\Omega \Psi(\boldsymbol{C})d\Omega_{Exact}}{\int_\Omega \Psi(\boldsymbol{C})d\Omega_{Exact}}} \times 100$$

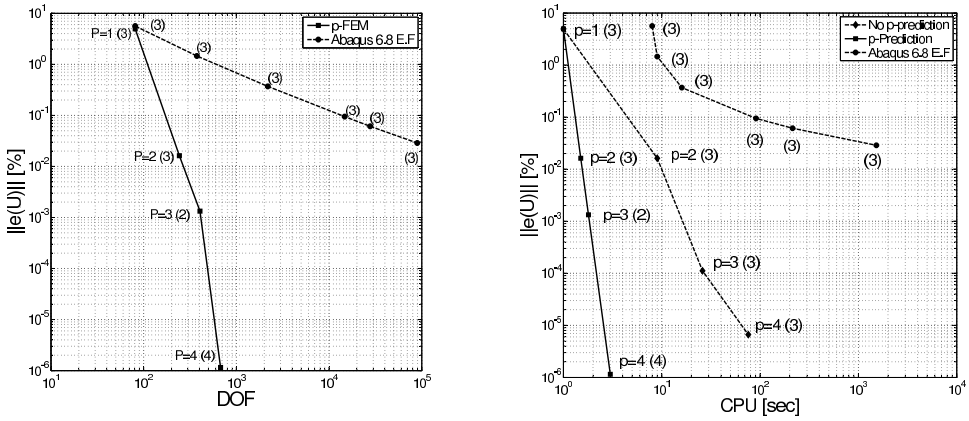

Figure 12: Relative error in energy norm as a function of DOFs (left) and CPU with and without the p-prediction algorithm (right) for the cube problem (number of load steps and average number of equilibrium iterations shown in brackets).

One may observe that the p-FEM is orders of magnitude faster in terms of DOFs compared to its h-FEM counterpart, and at least one to two orders of magnitude faster in terms of computational times.

Similar problems with an analytical solution for the verification of the p-FE implementation of the passive and active response are provided in [18, 15].

3.3. The active-passive response of an artery-like tube

The coupled passive-active mechanical response (7) of an artery-like domain made of two layers, media and adventitia, is investigated. The inner and outer diameter and media thickness is estimated from an in-vivo study of the abdominal aorta, having $D_{in} = 10$ mm, $D_{out} = 12.6$ mm, $h_{media} = 0.866$ mm, $h_{adventitia}/h_{media} = 2/3$, and length of $L = 20$ mm. The tube is clamped at both ends and loaded by an internal physiological pressure of $P = 13.33$ kPa (100 mmHg).

Collagen fibers are orientated at the angles $\pm\beta_M$ with respect to the circumferential direction and SMCs are wrapped in the media only in a circumferential direction (pitch angle $\beta_{MF} = 0$). Very little SMCs exist in the adventitia [34] so its mechanical response is purely passive. The material parameters for the passive and active response are given in Table 3. Because for each fiber at an angle β_M with respect to the circumferential direction, there is a fiber at an angle $-\beta_M$, and because the SMCs fibers are aligned along the

circumferential direction, circumferential symmetry is obtained (the "fibers" are not modeled, but only their homogenized contribution, so at each point there are 2 fibers at $\pm\beta_M$). Therefore only one eighth of the domain is discretized. Ten circular hexahedral elements graded towards the clamped boundary with symmetric boundary conditions are considered as shown in Figure 13.

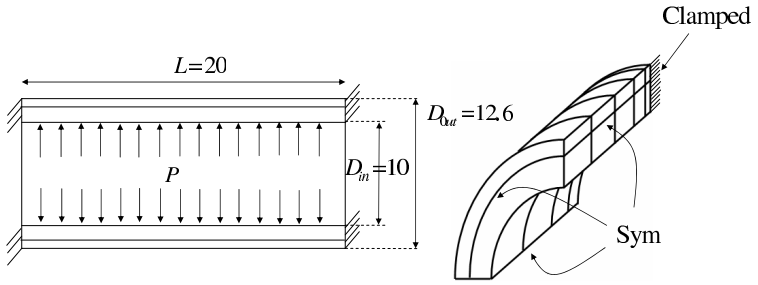

Figure 13: Mesh and boundary conditions for an artery-like structure with SMCs and collagen fibers.

Table 3: Material parameters fitted to a slightly compressible passive-active SEDF used in the FEA.

	c_1 $[MPa]$	D_1 $[MPa^{-1}]$	k_1 $[MPa]$	k_2	β_M $[^0]$	λ_0	λ_1	λ_m	m	EC_{50} $[mol/liter]$	S_{max} $[kPa]$
media	0.012	1.5	0.1	450	± 44	0.4	2.1	1.25	1	0.00075	222
adventitia	0.003	1.5	0.07	60	± 47	/	/	/	/	/	/

The value of D_1 in this example problem was chosen to be 1.5 $[MPa^{-1}]$ that although results in a relative volume change is about $\Delta V/V \approx 0.8\%$, still allows the use of the displacement formulation even for the h-version without the locking effect.

Since an analytical solution is unavailable for such a problem we computed a "benchmark" solution using 50 p-elements at $p = 8$ and 50% activation (basal tone), corresponding to a concentration value of $[A] = 7.5 \times 10^{-4}$. By using this solution as the reference solution, we plot in Figure 14 the estimated relative error in energy norm as a function of DOFs and CPU for p-and h-FEMs (we used the in-house p-FE code having blending mapping so with $p = 1$ and uniformly refine the mesh).

For comparison, if the same problem is solved with $D_1 = 0.15$ $[MPa^{-1}]$ instead (the material becomes progressively more incompressible), resulting

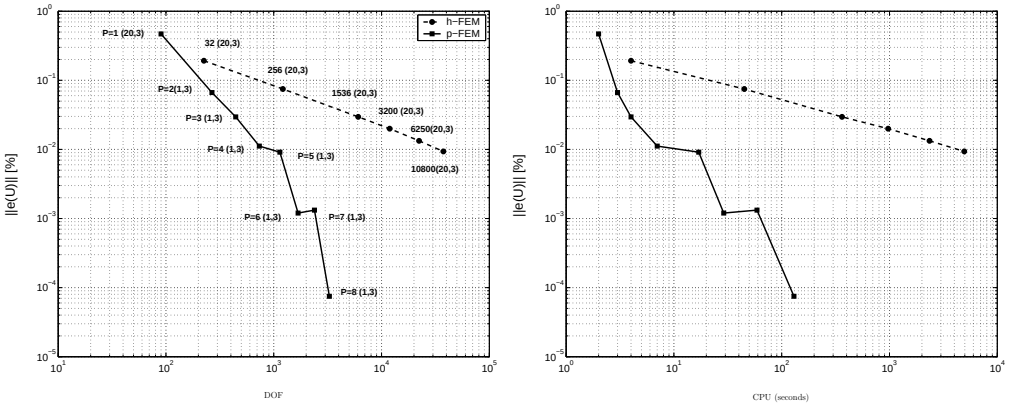

Figure 14: Estimated relative error in energy norm as a function of DOFs (left) and CPU with the p-prediction algorithm (right) for the bi-layer artery (number of load steps and average number of equilibrium iterations shown in brackets).

in a relative volume change of $\Delta V/V \approx 0.075\%$, then the displacement formulation of the h-FEM experience locking as shown in Figure 15. Comparing to Figure 14 one may observe that the p-FEM convergence is almost unaffected whereas the h-FEM convergence considerably deteriorates. In such

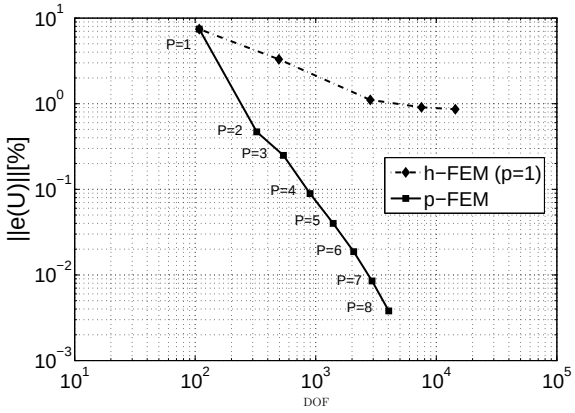

Figure 15: Estimated relative error in energy norm as a function of DOFs for the bi-layer artery with $D_1 = 0.15$ $[MPa^{-1}]$.

cases, it is well known that the hybrid formulation should be used for h-FEMs. A comparison between the performance of the p-FE implementation and the hybrid (mixed) formulation available in the commercial code Abaqus for a nearly incompressible artery-like structure is given in Appendix B.

To inspect the effect of the activation level, pure passive response, basal tone and saturation level are being considered, i.e., $[A] = 6.5 \times 10^{-9}, 7.5 \times 10^{-4}, 5 \times 10^{-2} [mol/liter]$. The circumferential stretch ratio and Cauchy stress across the artery wall thickness (at $x = L/2$) is computed and the effect of increased activation level on them is shown in Figure 16. One may observe

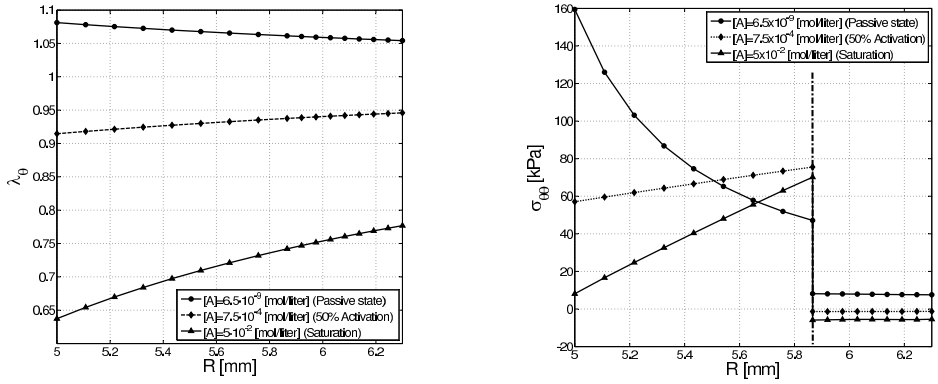

Figure 16: Circumferential stretch ratio (left) and Cauchy stress (right) across artery's wall at mid-length for different SMCs activation levels at $P = 100\ mmHg$. (right figure from [15].)

that at basal tone and at saturation the stretch ratios are smaller than 1, which means that the artery shrinks in diameter in comparison to the passive state. The active response "flattens" the stress distribution across the artery wall by decreasing the stress value at the inner boundary and increasing the value at the outer boundary, in accordance with available experimental observations on animal arteries. The flattening of the stress distribution is well know and has been documented for a one layer model in several works like [19, 35].

4. Summary and Conclusions

Several unique features of p-FEMs strongly advocate their use in the field of biomechanics and may enhance FEMs' use for patient-specific clinical treatment on a daily basis. Since the numerical errors are verified intrinsically one may focus the attention to the validation process and investigate the complex constitutive models of bones and arteries. Thanks to the fast convergence of the numerical results compared to classical FEMs (by at least

one order of magnitude faster in computational time), and the possible use of distorted FE meshes that may contain elements with high aspect ratios, it is easier to construct models and thus investigate more complex mathematical descriptions of the human organs.

For any patient-specific human femur, being an inhomogeneous elastic organ, the complete work-flow that may predict its mechanical response under loading has been developed, verified and tested by in-vitro experimentation, and to the author's opinion is ready for in-vivo clinical trials in an attempt to be used on a daily clinical basis.

The use of p-FEMs has been extended here to thin-layers, anisotropic, hyperelastic materials that may represent human arteries by strain-energy-density-functions which include both active and passive parts. p-FEMs were demonstrated for the first time (to the author's knowledge) to be orders of magnitude faster than h-FEMs both in respect to DOFs and CPU for these non-linear problems. Since not many experimental observations are available on arterial human tissues, we concentrated our attention on the verification procedures and the efficiency of p-FEMs when applied to artery-like structured made of thin layers. Similarly to the investigation of the human femur, these capabilities will be combined in the future with a patient-specific model generation of arteries and a set of in-vitro experiments to have a verified and validated method.

Acknowledgements

The author thanks two of his graduate students, Mr. Nir Trabelsi and Mr. Elad Priel for their assistance in preparing this manuscript. Four figures in this manuscript and Appendix B are from their PhD dissertation.

The author gratefully acknowledges the support of the Technische Universität München Institute for Advanced Study, funded by the German Excellence Initiative, and the Chief Scientist Office of the Ministry of Health, Israel, for their financial support for the research on bones.

Appendix A. Constitutive equations for arteries

Let us define the deformation gradient $\boldsymbol{F} = \mathrm{Grad}\ \boldsymbol{\varphi}(\boldsymbol{X}, t)$
$= \partial\varphi^k(X^1, X^2, X^3, t)/\partial X^K \boldsymbol{g}_i \otimes \boldsymbol{G}^K$, where $\boldsymbol{x} = \boldsymbol{\varphi}(\boldsymbol{X}, t)$ defines the placement of the point $\boldsymbol{X}$ at time t. X^K, $k = 1, 2, 3$, are the material (reference) (curvilinear) coordinates, $\boldsymbol{g}_i$ are the tangent and $\boldsymbol{G}^K$ the gradient vectors in the current and the reference configuration. Usually, the displacement

vector $\boldsymbol{U}(\boldsymbol{X},t) \stackrel{\text{def}}{=} (U_X, U_Y, U_Z)^T$ is introduced, i.e. $\boldsymbol{x} = \boldsymbol{X} + \boldsymbol{U}(\boldsymbol{X},t)$, and with this notation $\boldsymbol{F} = \boldsymbol{I} + \text{Grad } \boldsymbol{U}(\boldsymbol{X},t)$. We interchange X^1, X^2, X^3 with X, Y, Z when appropriate for the Cartesian coordinate system. A general strain-energy density function (SEDF) for an isotropic hyperelastic material with two families of fibers used to model the passive response is denoted by, $\psi_{passive}(\boldsymbol{C}, \hat{\boldsymbol{M}}_0, \hat{\boldsymbol{M}}_1) = \Psi_{passive}(\mathrm{I}_{\boldsymbol{C}}, \mathrm{II}_{\boldsymbol{C}}, \mathrm{III}_{\boldsymbol{C}}, \mathrm{IV}_{\boldsymbol{C}}, \mathrm{VI}_{\boldsymbol{C}})$, following [16]. It depends on the invariants of the right Cauchy-Green tensor $\boldsymbol{C} = \boldsymbol{F}^T\boldsymbol{F} = (\boldsymbol{I} + \text{Grad}\boldsymbol{U})^T(\boldsymbol{I} + \text{Grad}\boldsymbol{U})$, and the two unit direction vectors along collagen fiber directions $\hat{\boldsymbol{M}}_0$, and $\hat{\boldsymbol{M}}_1$.

The invariants of the Cauchy-Green tensor are

$$\mathrm{I}_{\boldsymbol{C}} = tr\boldsymbol{C}, \qquad \mathrm{II}_{\boldsymbol{C}} = \frac{1}{2}((tr\boldsymbol{C})^2 - tr\boldsymbol{C}^2), \qquad \mathrm{III}_{\boldsymbol{C}} = \det \boldsymbol{C} = (\det \boldsymbol{F})^2 \stackrel{\text{def}}{=} J^2, \tag{A.1}$$

where $tr\boldsymbol{C}$ symbolizes the trace operator and the invariants that represent stretch in the fiber directions are

$$\mathrm{IV}_{\boldsymbol{C}} = \hat{\boldsymbol{M}}_0 \cdot \boldsymbol{C} \cdot \hat{\boldsymbol{M}}_0, \qquad \mathrm{VI}_{\boldsymbol{C}} = \hat{\boldsymbol{M}}_1 \cdot \boldsymbol{C} \cdot \hat{\boldsymbol{M}}_1, \tag{A.2}$$

We consider a strain-energy density function composed of three parts for modeling the passive response, an isochoric isotropic and a volumetric isotropic Neo-Hookean parts representing the elastic matrix, and a transversely isotropic part representing the collagen fibers in the artery wall

$$\Psi_{passive} = [\Psi_{isoch}(\mathrm{I}_{\boldsymbol{C}}, \mathrm{III}_{\boldsymbol{C}}) + \Psi_{vol}(\mathrm{III}_{\boldsymbol{C}})] + \Psi_{fibers}(\mathrm{IV}_{\boldsymbol{C}}, \mathrm{VI}_{\boldsymbol{C}}), \tag{A.3}$$

The isochoric isotropic and volumetric isotropic parts are represented by a nearly incompressible Neo-Hookean SEDF:

$$\Psi_{isoch} = c_1(\mathrm{I}_{\boldsymbol{C}}\mathrm{III}_{\boldsymbol{C}}^{-1/3} - 3), \quad \Psi_{vol} = \frac{1}{D_1}(\mathrm{III}_{\boldsymbol{C}}^{1/2} - 1)^2 \tag{A.4}$$

c_1 and D_1 are constants related to the shear modulus μ and to the bulk modulus κ

$$c_1 = \frac{\mu}{2}, \qquad D_1 = \frac{2}{\kappa}. \tag{A.5}$$

The transversely isotropic part for modelling the collagen fiber contribution is [16]:

$$\begin{aligned} \Psi_{fibers} = &\frac{k_1}{2k_2}\left[\exp\left[k_2\left(\mathrm{IV}_{\boldsymbol{C}} - 1\right)^2\right] - 1\right] \\ &+ \frac{k_1}{2k_2}\left[\exp\left[k_2\left(\mathrm{VI}_{\boldsymbol{C}} - 1\right)^2\right] - 1\right], \quad \mathrm{IV}_{\boldsymbol{C}}, \mathrm{VI}_{\boldsymbol{C}} \geq 1 \end{aligned} \tag{A.6}$$

To model the active response we construct a SEDF based on [19]. The first Piola-Kirchhoff stress component due to smooth muscle cells (SMCs) contraction was found to be proportional to the concentration of the vasoconstrictor $[A]$, as well as the stretch ratio in the SMCs-fibers direction $\hat{\boldsymbol{M}}_{MF}$, denoted by λ_f:

$$P_{ff}^{active} = S([A])f(\lambda_f) \tag{A.7}$$

where $S([A])$ is the tension-dose relationship and $f(\lambda_f)$ is the tension-stretch relation. The tension-dose relationship is usually available from ring-tests, as given in [36], so that:

$$S([A]) = S_{max}\frac{[A]^m}{[A]^m + EC_{50}^m} \tag{A.8}$$

where m is the slope parameter, S_{max} the maximum value of contraction and EC_{50} being the concentration at which 50% of maximum generated tension is obtained. In Figure A.17 a representative tension-dose relation is presented. Figure A.17 shows that under a vasoconstrictor threshold concentration no

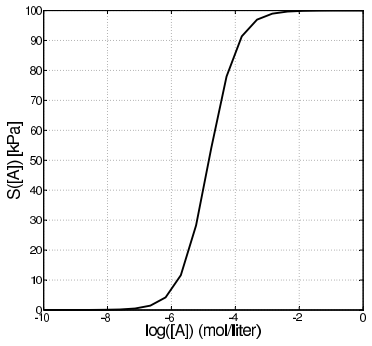

Figure A.17: Representative tension-dose relation using $EC_{50} = 0.000015$ $[mol/liter]$,$m = 1$ taken from [36] and $S_{max} = 100$ kPa taken from [19].

induced active response is generated and on the other end the active response reaches a saturation level beyond a given vasoconstrictor concentration.

The tension-stretch relation is adopted from the work in [19]:

$$f(\lambda_f) = \begin{cases} \left[1 - \left(\frac{\lambda_m - \lambda_f}{\lambda_m - \lambda_0}\right)^2\right], & \lambda_1 > \lambda_f > \lambda_0 \\ 0, & Otherwise \end{cases} \tag{A.9}$$

with λ_m being the stretch at which maximum contraction is possible and λ_0 and $\lambda_1 = \lambda_0 + 2(\lambda_m - \lambda_0)$ being the minimum and maximum stretch at which contraction can be generated. Using (A.8), (A.9) and (A.7), and defining the direction of the SMCs before deformation by $\hat{\boldsymbol{M}}_{MF}$ (with a corresponding angle β_{SMC}) we may obtain an expression for the active SEDF Ψ_{active}:

$$\Psi_{active} = \begin{cases} S_{max} \frac{[A]^m}{[A]^m + EC_{50}^m} \left[\frac{(\lambda_m - \sqrt{\mathrm{IV}_{\boldsymbol{C}}^{MF}})^3}{3(\lambda_m - \lambda_0)^2} + \sqrt{\mathrm{IV}_{\boldsymbol{C}}^{MF}} \right], & \lambda_1^2 > \mathrm{IV}_{\boldsymbol{C}}^{MF} > \lambda_0^2 \\ 0, & Otherwise \end{cases} \tag{A.10}$$

The dependency of Ψ_{active} on $\mathrm{IV}_{\boldsymbol{C}}^{MF}$ assures that the active stress is in the SMCs direction only with zero components perpendicular to it.

Appendix B. An almost incompressible artery: *p*-FEA compared to Abaqus hybrid(mixed) *h*-FEA

In this appendix the performance of the "displacement formulation" of the p-FEM for a nearly incompressible artery is compared to the hybrid formulation used in Abaqus for an incompressible artery. Because only the "incompressible" passive implementation is available in Abaqus (same formulation as in (A.4) and (A.6)) we use it for the simulation of a LAD coronary artery. The material parameters for (A.5) and (A.6) were fitted by Gasser et al. [37] to experimental data on the human LAD coronary artery reported by Carmines et al. [38] and are summarized (with each layer's radii) in Table B.4 In the p-FE analysis a value of $D_1 = 0.01\ MPa^{-1}$ was used

Table B.4: Material parameters fitted to a LAD human coronary arteries according to [37].

Layer	$c_1[kPa]$	$k_1[kPa]$	k_2	$\pm\beta_M$ [deg]	$R_{in}[mm]$	$R_{out}[mm]$
Media	27	0.64	3.54	10	3.3170	3.8103
Adventitia	2.7	5.1	15.4	40	3.8103	4.0570

to ensure that $J - 1 = \frac{\triangle V}{V} \approx 0.001\%$. The artery was modeled as a tube of length $L = 20\ mm$, clamped at both ends and loaded by an internal pressure of $P = 13.3\ \ kPa(100\ mmHg)$. Due to problem's symmetry, an eight of the tube was modeled with symmetry boundary conditions applied as shown in Figure B.18. The "benchmark" solution was obtained using a graded mesh model with 100 hexahedral elements (see Figure B.18) having at

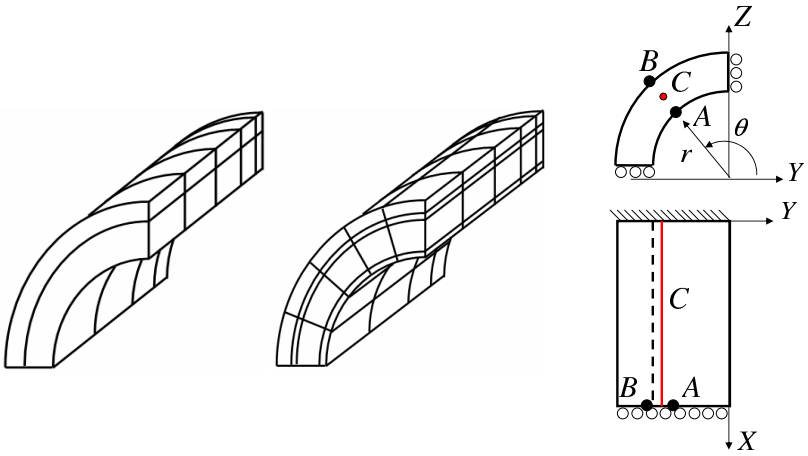

Figure B.18: Left - p-FE mesh used in our analyses. Middle - refined p-FE mesh used for the benchmark solution. Right - Boundary conditions and locations at which data was extracted.

$p = 8$ 54720 $DOFs$. The problem was also solved using hybrid(mixed) h-FE elements (the commercial code Abaqus 6.8 EF). An example of the meshes used for Abaqus analysis are shown in Figure B.19. The elements have a maximum aspect ratio of 1:4 thus a large number of elements are obtained for thin layered structures such as the artery wall. Eight-noded hexahedral

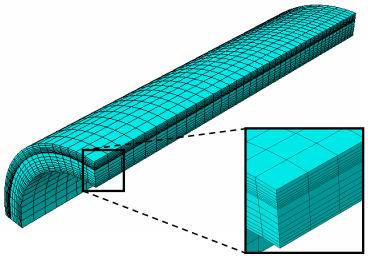

Figure B.19: The h-FE mesh (used by Abaqus).

hybrid elements were used due to the incompressibility constraint (20-noded quadratic hexahedral elements were also tested showing same efficiency as the 8-noded ones) and an automatic load step control was utilized in the non-linear iterative scheme. Convergence in relative error in strain energy for the "benchmark" solution is shown in Figure B.20.

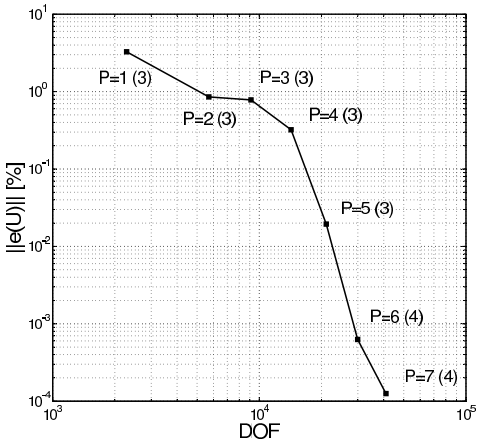

Figure B.20: Relative error in energy norm (average number of equilibrium iterations shown in brackets).

In Figures B.21 and B.22 the convergence of the radial displacement and circumferential stress at point A and B are presented. The convergence rates of the p-FEMs with respect to DOFs and CPU are much faster compared to their h-FEM counterparts. This is especially important when modeling a general artery constructed from multiple thin layers. In Figure B.23 an example of the circumferential stress plot obtained for ABAQUS (28650 elements) and by p-FEMs (10 elements with $p = 4$) is shown. The "mesh" in the figure is the visualization mesh. Due to the slow convergence rate of the h-FEM if one would conduct a standard convergence test of the stress the results may be misleading. Comparing the circumferential stress at point B for a mesh of 15840 elements (point 6 in Figure B.22) to a finer mesh of 21000 elements (point 7 in Figure B.22) one obtains a difference of 0.89% which seems to be within less than $< 1\%$ when in fact the actual error for the 15840 element mesh is $\approx 6\%$.

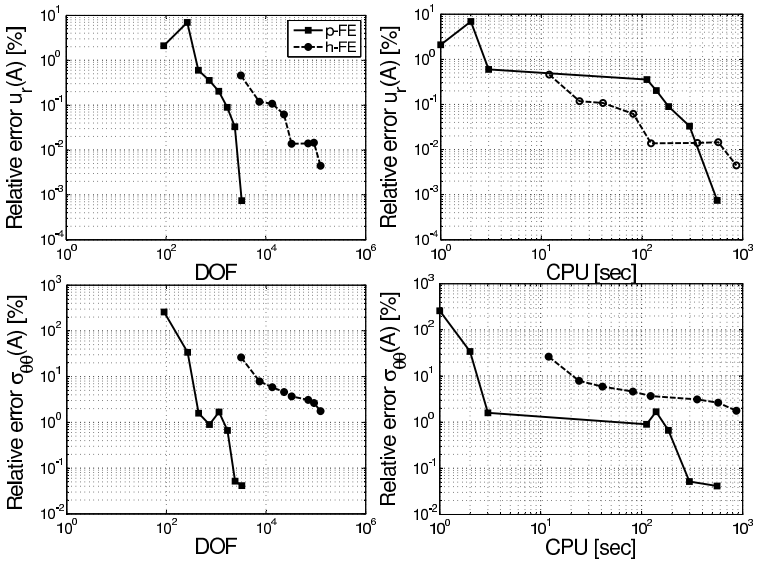

Figure B.21: Relative error in radial displacement u_r and circumferential stress $\sigma_{\theta\theta}$at point A.

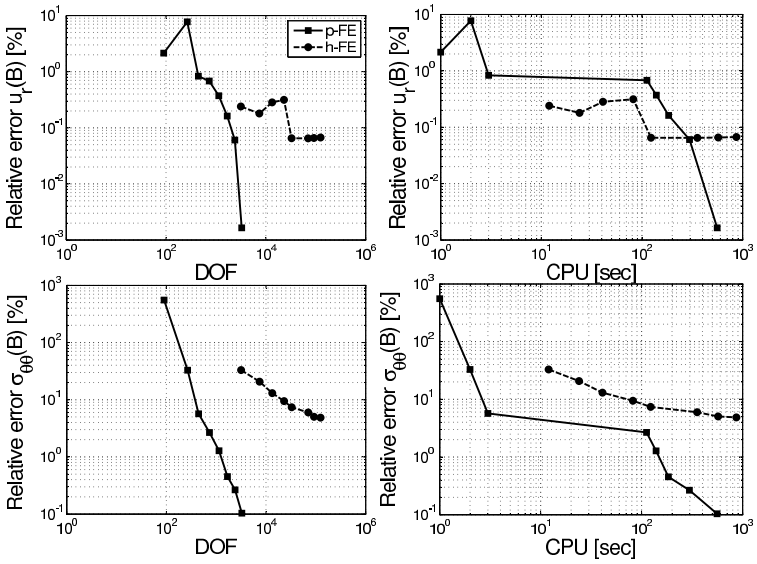

Figure B.22: Relative error in radial displacement u_r and circumferential stress $\sigma_{\theta\theta}$ at point B.

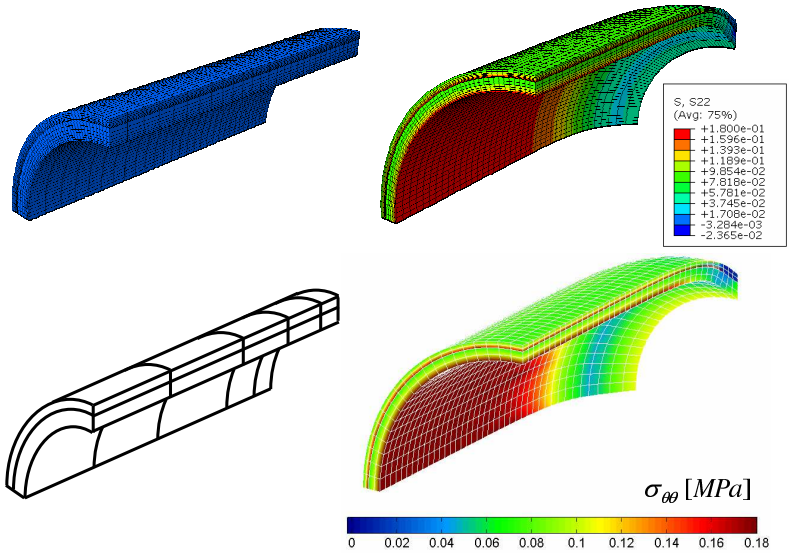

Figure B.23: Left - Mesh used for computations Abaqus (Top) and our p-FE code (Bottom). Right - Circumferential stress $\sigma_{\theta\theta}$ plot for bi-layered artery Abaqus (Top) and our p-FE code (Bottom).

References

[1] B. A. Szabó, I. Babuška, Finite Element Analysis, John Wiley & Sons, New York, 1991.

[2] S. M. Holzer, Z. Yosibash, The p-version of the finite element method in incremental elasto-plastic analysis, Int. Jour. Numer. Meth. Engrg. 39 (1996) 1859–1878.

[3] A. Düster, E. Rank, A p-version finite element approach for two- and three-dimensional problems of the J_2 flow theory with non-linear isotropic hardening, Int. Jour. Numer. Meth. Engrg. 53 (2002) 49–63.

[4] A. Düster, S. Hartmann, E. Rank, p-FEM applied to finite isotropic hyperelastic bodies, Computer Meth. Appl. Mech. Engrg. 192 (2003) 5147–5166.

[5] U. Heisserer, S. Hartmann, A. Düster, Z. Yosibash, On volumetric locking-free behavior of p-version finite elements under finite deformations, Communications Numer. Meth. Engrg. 24 (11) (2008) 1019–1032.

[6] J. H. Keyak, J. M. Meagher, H. B. Skinner, J. C. D. Mote, Automated three-dimensional finite element modelling of bone: A new method, ASME Jour. Biomech. Eng. 12 (1990) 389–397.

[7] F. Taddei, E. Schileo, B. Helgason, L. Cristofolini, M. Viceconti, The material mapping strategy influences the accuracy of CT-based finite element models of bones: An evaluation against experimental measurements, Med. Eng. Phys. 29 (9) (2007) 973–979.

[8] E. Schileo, E. DallAra, F. Taddei, A. Malandrino, T. Schotkamp, M. Baleani, M. Viceconti, An accurate estimation of bone density improves the accuracy of subject-specific finite element models, Jour. Biomech. 41 (2008) 2483–2491.

[9] U. Pise, A. Bhatt, R. Srivastava, R. Warkedkar, A B-spline based heterogeneous modeling and analysis of proximal femur with graded element, Jour. Biomech. 42 (2009) 1981 – 1988.

[10] C. Hellmich, C. Kober, B. Erdmann, Micromechanics-based conversion of CT data into anisotropic elasticity tensors, applied to FE simulations of a mandible, Annals of Biomedical Engineering 36 (2008) 108–122.

[11] Z. Yosibash, N. Trabelsi, C. Hellmich, Subject-specific p-FE analysis of the proximal femur utilizing micromechanics based material properties, Int. Jour. Multiscale Computational Engineering 6 (5) (2008) 483–498.

[12] N. Trabelsi, Z. Yosibash, Patient-specific FE analyses of the proximal femur with orthotropic material properties validated by experiments, ASME Jour. Biomech. Eng. 155 (2011) 061001–1 – 061001–11.

[13] N. Trabelsi, Z. Yosibash, C. Wutte, R. Augat, S. Eberle, Patient-specific finite element analysis of the human femur - a double-blinded biomechanical validation, Jour. Biomech. 44 (2011) 1666 – 1672.

[14] Z. Yosibash, S. Hartmann, U. Heisserer, A. Duester, E. Rank, M. Szanto, Axisymmetric pressure boundary loading for finite deformation analysis using p-FEM, Computer Meth. Appl. Mech. Engrg. 196 (2007) 1261 1277.

[15] Z. Yosibash, E. Priel, Artery active mechanical response: High order finite element implementation and investigation, Computer Meth. Appl. Mech. Engrg. 237 - 240 (2012) 51 – 66.

[16] G. Holzapfel, T. Gasser, R. Ogden, A new constitutive framework for arterial wall mechanics and a comparative study of material models, Jour. Elasticity 61 (2000) 1–48.

[17] G. Holzapfel, R. Ogden, Constitutive modelling of arteries, Proc. R. Soc. A 466 (2010) 15511597.

[18] Z. Yosibash, E. Priel, p-FEMs for hyperelastic anisotropic nearly incompressible materials under finite deformations with applications to arteries simulation, Int. Jour. Numer. Meth. Engrg. 88 (2011) 1152–1174.

[19] A. Rachev, K. Hayashi, Theoretical study of the effects of vascular smooth muscle contraction on strain and stress distributions in arteries, Annals of Biomedical Engineering 27 (4) (1999) 459–468.

[20] K. Hibbitt, S. Inc., ABAQUS manual version 6.82EF, 2009.

[21] Z. Yosibash, N. Trabelsi, C. Milgrom, Reliable simulations of the human proximal femur by high-order finite element analysis validated by experimental observations, Jour. Biomech. 40 (2007) 3688–3699.

[22] D. Carter, W. Hayes, The compressive behavior of bone as a two-phase porous structure, Jour. Bone Joint Surg. 59 (1977) 954–962.

[23] D. D. Cody, F. J. Hou, G. W. Divine, D. P. Fyhrie, Short term in vivo study of proximal femoral finite element modeling, Annals Biomedical Eng. 28 (2000) 408–414.

[24] J. Keyak, Y. Falkinstein, Comparison of in situ and in vitro CT scan-based finite element model predictions of proximal femoral fracture load, Med. Eng. Phys. 25 (2003) 781–787.

[25] T. S. Keller, Predicting the compressive mechanical behavior of bone, Jour. Biomech. 27 (1994) 1159–1168.

[26] E. F. Morgan, H. H. Bayraktar, T. M. Keaveny, Trabecular bone modulus-density relationships depend on anatomic site, Jour. Biomech. 36 (2003) 897–904.

[27] N. Trabelsi, Z. Yosibash, C. Milgrom, Validation of subject-specific automated p-FE analysis of the proximal femur, Jour. Biomech. 42 (2009) 234–241.

[28] Z. Yosibash, R. Padan, L. Joscowicz, C. Milgrom, A CT-based high-order finite element analysis of the human proximal femur compared to in-vitro experiments, ASME Jour. Biomech. Eng. 129 (3) (2007) 297–309.

[29] C. Cann, Quantitative CT for determination of bone mineral density: A review, Radiology 166 (1988) 509–522.

[30] F. Taddei, L. Cristofolini, S. Martelli, H. Gill, M. Viceconti, Subject-specific finite element models of long bones: An in vitro evaluation of the overall accuracy, Jour. Biomech. 39 (2006) 2457–2467.

[31] J. Bonet, R. Wood, Nonlinear continuum mechanics for finite element analysis, Cambridge university press, USA, 1997.

[32] A. Duster, High order finite elements for three dimensional, thin-walled nonlinear continua, Ph.D. thesis, Technische Universität München, Munich, Germany (2001).

[33] W. Press, B. Flannery, S. Teukolsky, W. Vetterling, Numerical Recipes: The art of scientific computing, Cambridge University Press, 1986.

[34] B. Levy, A. Tedgui, Biology of the arterial wall, Kluwer Academic Publishers, 1999.

[35] H. Wagner, J. Humphrey, Differential passive and active biaxial mechanical behavior of muscular and elastic arteries: Basilar versus common carotid, Jour. Biomech. Eng. 133, article number: 051009.

[36] P. Chamiot-Clerc, X. Copie, J. Renaud, M. Safer, X. Girerd, Comparative reactivity amd mechanical properties of human isolated internal mammary and radial arteries, Cardiovascular Resrearch 37 (1998) 811–819.

[37] T. Gasser, C. Schulz-Bauer, G. Holzapfel, A three dimensional finite element model for arterial clamping, Jour. Biomech. Eng. 124 (2002) 355–363.

[38] D. Carmines, J. McElhaney, R. Stack, A piecewise non-linear elastic stress-expression of human and pig coronary arteries tested in-vitro, Jour. Biomech. 24 (1991) 899–906.